Petroleum Science 18 (2021) 1675–1688

Contents lists available at ScienceDirect

Petroleum Science

journal homepage: www.keaipublishing.com/en/journals/petroleum-science

Original Paper

Estimation of fracture density and orientation from azimuthal elastic impedance difference through singular value decomposition

Lin Li [a, *], Guang-Zhi Zhang [a, **], Jun-Zhou Liu [b], Lei Han [b], Jia-Jia Zhang [a]

[a] School of Geosciences, China University of Petroleum (East China), Qingdao, Shandong 266580, China
[b] Sinopec Exploration and Production Research Institute, Beijing, 100083, China

ARTICLE INFO

Article history:
Received 24 October 2020
Accepted 24 May 2021
Available online 21 September 2021

Edited by Jie Hao and Teng Zhu

Keywords:
Singular value decomposition
HTI media
Azimuthal elastic impedance inversion
Fracture density
Fracture orientation

ABSTRACT

Accurate estimation of fracture density and orientation is of great significance for seismic characterization of fractured reservoirs. Here, we propose a novel methodology to estimate fracture density and orientation from azimuthal elastic impedance (AEI) difference using singular value decomposition (SVD). Based on Hudson's model, we first derive the AEI equation containing fracture density in HTI media, and then obtain basis functions and singular values from the normalized AEI difference utilizing SVD. Analysis shows that the basis function changing with azimuth is related to fracture orientation, fracture density is the linearly weighted sum of singular values, and the first singular value contributes the most to fracture density. Thus, we develop an SVD-based fracture density and orientation inversion approach constrained by smooth prior elastic parameters. Synthetic example shows that fracture density and orientation can be stably estimated, and the correlation coefficient between the true value and the estimated fracture density is above 0.85 even when an S/N ratio of 2. Field data example shows that the estimated fracture orientation is consistent with the interpretation of image log data, and the estimated fracture density reliably indicates fractured gas-bearing reservoir, which could help to guide the exploration and development of fractured reservoirs.

1. Introduction

Natural fractures developed in reservoirs are closely related to fluid flow properties. Fracture density (or crack density) and orientation are the key parameters for characterizing fractures in a reservoir, a high density of naturally open fractures could provide channels with high permeability for fluid, and fracture orientation may control the direction of fluid flow. Knowledge of fracture density and orientation is of great significance for the optimization of well placement and drilling direction of horizontal wells (Liu and Martinez, 2013).

Post-stack geometric seismic attributes (coherence, curvature, ant-tracking, etc.) allow for qualitatively characterizing faults and indirectly delineating fractures (Chopra and Marfurt, 2007; Liu et al., 2011). Recently, fracture-induced azimuthal anisotropy estimate becomes an effective tool for seismic characterization of a fractured reservoir. Fitting an ellipse to various azimuthal seismic attributes (amplitude, velocity, attenuation, Young's modulus, etc.) is a feasible method for fracture development intensity and fracture orientation estimates (Mallick et al., 1998; Grechka and Tsvankin, 1999; Al-Marzoug et al., 2006; Zong et al., 2018; Chen et al., 2018). However, a quantitative characterization of fractures requires modeling seismic response given the prior rock properties of fractured rock. With the development of the seismic acquisition and processing technology, fracture detection by pre-stack seismic inversion combing with effective medium theories becomes a topic of increased interest due to the potential in extracting quantitatively fracture properties from pre-stack 5D seismic data (Yin et al., 2018). Hudson's model (1981) and Schoenberg's linear slip model (1980) are two classic models for simulating subsurface fractures, and they are equivalent under the low-frequency assumption (Bakulin et al., 2000). Hudson's model assumes that fractures are aligned isolated penny-shaped cracks, while Schoenberg's linear slip model treats fractures as imperfectly bonded interfaces. Considering the simple case that isotropic overlying horizontal transverse isotropy (HTI) media induced by aligned vertical

* Corresponding author.
** Corresponding author.
E-mail addresses: lilinupc@126.com (L. Li), zhanggz@upc.edu.cn (G.-Z. Zhang).

https://doi.org/10.1016/j.petsci.2021.09.037

fractures (Rüger, 1997), several authors proposed to obtain fracture development intensity by extracting anisotropic gradient based on Rüger's approximation (Sun et al., 2011; Zhang et al., 2012; Li et al. 2017, 2018; Liu et al., 2018). Downton et al. (2011) rewrote azimuthal P-wave reflectivity in terms of Fourier coefficients (FCs) and presented the second FC as a scaled anisotropic gradient. Furthermore, methods estimating fracture weaknesses from azimuthal seismic data based on Schoenberg's linear slip model were reported in several papers (Chen et al., 2015; Downton and Roure, 2015; Pan et al., 2018; Pan and Zhang, 2019; Li et al., 2020).

Singular value decomposition (SVD) has been successfully applied to image denoising processing, AVO attribute prediction (Causse et al., 2007a), and pore fluid and lithofacies classification (Causse et al., 2007b). Zong et al. (2013) developed the damping SVD method to enhance the estimation stability of Young's modulus and Poisson's ratio. Yuan et al. (2020) presented to use SVD to calculate the azimuthal anisotropy among 6D phase-difference attributes. Varela et al. (2007) and Varela (2009) proposed to extract fracture density using the weights derived from SVD of the azimuthal reflection coefficient, which is applicable for the case of an isotropic layer over an HTI halfspace. However, for the case where the upper and lower layers are both HTI media, the inversion result is the difference in fracture density across the boundary, but not fracture density. In addition, the inversion is highly dependent on the prior model parameters (P- and S-wave velocities and density).

Here, we extend the approach proposed by Varela et al. (2007) and Varela (2009) to HTI media with the same symmetry axis orientation and propose a novel methodology to estimate fracture density and orientation from azimuthal elastic impedance (AEI) difference using SVD. We first derive the AEI equation containing fracture density in HTI media using the relationship between fracture density and fracture weaknesses for gas-filled fractures. To reduce the influence of the isotropic background and highlight the contribution of the fracture density term, we then present to perform SVD on the normalized AEI difference to obtain SVD attributes (basis functions and singular values). Next, we analyze the relationship between fracture density, fracture orientation, and SVD attributes, and propose a complete workflow to estimate fracture density and orientation from these SVD attributes. Finally, the proposed approach is validated by synthetic and field data examples.

2. Theory and method

2.1. AEI equation with fracture density

Schoenberg (1980) modeled fractures as imperfectly bonded interfaces and assumed that the stress along these interfaces is continuous, while the displacement is not continuous, and linear tangential slip occurs. Furthermore, Schoenberg and Sayers (1995) introduced two non-negative dimensionless fracture parameters (normal δ_N and tangential δ_T weaknesses), which are used to model the seismic response of fractured reservoirs. Pan et al. (2017) rewrote the Rüger's approximation (1998) in terms of fracture weaknesses, which is given by

$$R(\theta,\varphi)=\frac{1}{2}a(\theta)\frac{\Delta\alpha}{\alpha_0}+\frac{1}{2}b(\theta)\frac{\Delta\beta}{\beta_0}+\frac{1}{2}c(\theta)\frac{\Delta\rho}{\rho_0}+\frac{1}{2}d(\theta,\varphi)\Delta\delta_N+\frac{1}{2}e(\theta,\varphi)\Delta\delta_T \tag{1}$$

with

$$a(\theta)=\sec^2\theta$$

$$b(\theta)=-8g\sin^2\theta$$

$$c(\theta)=1-4g\sin^2\theta$$

$$d(\theta,\varphi)=-2g\Big[\times\left(\cos^2\varphi\sin^2\theta+\sin^2\varphi\cos^2\varphi\sin^2\theta\tan^2\theta\right)(1-2g)+\left(\cos^4\varphi\sin^2\theta\tan^2\theta\right)(1-g)\Big]$$

$$e(\theta,\varphi)=2g\cos^2\varphi\sin^2\theta-2g\sin^2\varphi\cos^2\varphi\sin^2\theta\tan^2\theta$$

where, α, β, and ρ represent P- and S-wave velocities, and density in the isotropic background; The subscript 0 denotes the average value across the boundary; $g\equiv\beta_0^2/\alpha_0^2$ represents the squared S-to-P-wave velocity ratio; $\Delta\delta_N$ and $\Delta\delta_T$ are the differences of the normal and tangential weaknesses across the boundary; θ is the incident angle; φ is azimuth between the source-receiver-line azimuth ϕ and the fracture symmetry axis azimuth ϕ_{sym}.

In seismic exploration, geophysicists often use fracture or crack density for fracture characterization. Hudson (1981) modeled cracks as 'penny' shape and defined fracture density as:

$$e=\frac{Kr^3}{V} \tag{2}$$

where K/V is the number of cracks per unit volume, r is the average radius of cracks.

Bakulin et al. (2000) derived the relationship between fracture density and fracture weaknesses. For dry or gas-filled cracks:

$$\delta_N=\frac{4e}{3g(1-g)} \tag{3}$$

$$\delta_T=\frac{16e}{3(3-2g)} \tag{4}$$

For very flat cracks (with very small aspect ratio) filled with fluid, which gives:

$$\delta_N=0 \tag{5}$$

$$\delta_T=\frac{16e}{3(3-2g)} \tag{6}$$

Here, we mainly focus on the case of gas-filled cracks. Substituting equations (3) and (4) into equation (1) to give:

$$R(\theta,\varphi)=\frac{1}{2}a(\theta)\frac{\Delta\alpha}{\alpha_0}+\frac{1}{2}b(\theta)\frac{\Delta\beta}{\beta_0}+\frac{1}{2}c(\theta)\frac{\Delta\rho}{\rho_0}+\frac{1}{2}f(\theta,\varphi)\Delta e \tag{7}$$

where Δe represents the difference in fracture density across the boundary,

$$f(\theta,\varphi)=\left[\frac{4(2g-1)}{3(1-g)}+\frac{16g}{3(3-2g)}\right]\cos2\varphi\sin^2\theta+\left[-\frac{4}{3}\cos2\varphi+\frac{g(1-2g)}{3(3-2g)(1-g)}\cos4\varphi\right]\sin^2\theta\tan^2\theta$$

Azimuthal reflection coefficient could be deduced from AEI using the logarithmic approximation (Connolly, 1999; Martins, 2006):

$$R(\theta,\varphi)=\frac{\Delta EI(\theta,\varphi)}{2EI(\theta,\varphi)}\approx\frac{1}{2}\ln EI(\theta,\varphi) \tag{8}$$

Combining equations (7) and (8), we derive the normalized AEI equation with fracture density:

$$EI(\theta,\varphi)=EI_0\left(\frac{\alpha}{\alpha_0}\right)^{a(\theta)}\left(\frac{\beta}{\beta_0}\right)^{b(\theta)}\left(\frac{\rho}{\rho_0}\right)^{c(\theta)}\exp[f(\theta,\varphi)e] \tag{9}$$

where EI_0 is the average of the EI log.

Taking the logarithms of both sides of equation (9), the linearized logarithmic AEI equation is given by (Whitcombe, 2002):

$$L_{EI}(\theta,\varphi)=a(\theta)L_P+b(\theta)L_S+c(\theta)L_D+f(\theta,\varphi)e \tag{10}$$

where, $L_{EI}(\theta,\varphi)=\ln\frac{EI(\theta,\varphi)}{EI_0}$,$L_P=\ln\frac{\alpha}{\alpha_0}$,$L_S=\ln\frac{\beta}{\beta_0}$,$L_D=\ln\frac{\rho}{\rho_0}$.

2.2. SVD of the normalized AEI difference

Varela et al. (2007) and Varela (2009) proposed to perform SVD on the azimuthal reflection coefficient to obtain the SVD seismic attributes, which is expressed as:

$$R(\theta,\varphi)=C_1(\theta,e)f_1(\varphi)+C_2(\theta,e)f_2(\varphi)+C_3(\theta,e)f_3(\varphi)+\ldots \tag{11}$$

where$f_i(\varphi)(i=1,2,3\ldots)$ represents basis function changing with azimuth; $C_i(i=1,2,3\ldots)$ represents weight changing with incident angle and rock properties (velocities, density, and fracture density); Varela et al. (2007) and Varela (2009) proposed to estimate fracture density from weights obtained from the SVD of the modeled and observed azimuthal reflection coefficients. The approach proposed by Varela et al. (2007) and Varela (2009) is applicable for the case of isotropic overlying HTI media. However, for the case where the upper and lower layers are both HTI media, the inversion result is the difference in fracture density across the boundary, but not fracture density. In addition, the inversion is highly dependent on the prior model parameters (P- and S-wave velocities and density).

Following Varela et al. (2007) and Varela (2009), we propose to perform SVD on the normalized AEI difference for fracture density and orientation estimates, which is applicable for HTI media with the same symmetry axis. Since the weight coefficients of the isotropic terms are much larger than that of the anisotropic term in equation (10), the effect of fracture density term on the AEI is not prominent (Pan et al., 2017). To reduce the influence of isotropic terms on fracture density inversion, the normalized AEI difference is calculated:

$$\begin{aligned}\Delta L_{EI}(\theta,\varphi)&=L_{EI}(\theta,\varphi)-L_{EI}(\theta,\varphi_0)\\&=[f(\theta,\varphi)-f(\theta,\varphi_0)]e\end{aligned} \tag{12}$$

where $\varphi_0=\phi_0-\phi_{\mathrm{sym}}$ represents the azimuth between the reference observed azimuth ϕ_0 and the fracture symmetry axis.

Performing SVD on equation (12) to give:

$$\Delta L_{EI}(\theta,\varphi)=f_1(\varphi)d_{11}(e)v_1(\theta)+f_2(\varphi)d_{22}(e)v_2(\theta)+f_3(\varphi)d_{33}(e)v_3(\theta)+\ldots \tag{13}$$

Here, different from the approach proposed by Varela et al. (2007) and Varela (2009), the weight $C_i(\theta,e)$ is decomposed into the product of the singular value $d_{ii}(e)$ and the basis function $v_i(\theta)$ changing with incident angle.

In the case of M azimuths and N incident angles, we rewrite equation (13) in matrix form as:

$$\mathbf{\Delta L_{EI}}=\mathbf{FDV}^{\mathrm{T}} \tag{14}$$

with,

$$\mathbf{\Delta L_{EI}}=\begin{bmatrix}\Delta L_{EI}(\varphi_1,\theta_1) & \Delta L_{EI}(\varphi_1,\theta_2) & \cdots & \Delta L_{EI}(\varphi_1,\theta_N)\\ \Delta L_{EI}(\varphi_2,\theta_1) & \Delta L_{EI}(\varphi_2,\theta_2) & \cdots & \Delta L_{EI}(\varphi_2,\theta_N)\\ \vdots & \vdots & & \vdots\\ \Delta L_{EI}(\varphi_M,\theta_1) & \Delta L_{EI}(\varphi_M,\theta_2) & \cdots & \Delta L_{EI}(\varphi_M,\theta_N)\end{bmatrix}_{M\times N}$$

$$\mathbf{F}=\begin{bmatrix}f_1(\varphi_1) & f_2(\varphi_1) & \cdots & f_M(\varphi_1)\\ f_1(\varphi_2) & f_2(\varphi_2) & \cdots & f_M(\varphi_2)\\ \vdots & \vdots & & \vdots\\ f_1(\varphi_M) & f_2(\varphi_M) & \cdots & f_M(\varphi_M)\end{bmatrix}_{M\times M}$$

$$\mathbf{V}=\begin{bmatrix}v_1(\theta_1) & v_2(\theta_1) & \cdots & v_N(\theta_1)\\ v_1(\theta_2) & v_2(\theta_2) & \cdots & v_N(\theta_2)\\ \vdots & \vdots & & \vdots\\ v_1(\theta_N) & v_2(\theta_N) & \cdots & v_N(\theta_N)\end{bmatrix}_{N\times N}$$

where, $\mathbf{F}$ $(M\times M)$ and $\mathbf{V}$ $(N\times N)$ are unit orthogonal matrices; The columns of $\mathbf{F}$ represent basis functions changing with azimuth, which are eigenvectors of $\Delta L_{EI}\Delta L_{EI}{}^{\mathrm{T}}$; The columns of $\mathbf{V}$ represent basis functions changing with incident angle, which are eigenvectors of $\Delta L_{EI}{}^{\mathrm{T}}\Delta L_{EI}$; $\mathbf{D}$ $(M\times N)$ is singular value matrix, the diagonals of $\mathbf{D}$ are singular values, which are square roots of the nonzero eigenvalues of $\Delta L_{EI}\Delta L_{EI}{}^{\mathrm{T}}$ and $\Delta L_{EI}{}^{\mathrm{T}}\Delta L_{EI}$. The symbol T represents the transpose of the matrix.

We set up a single-layer HTI model induced by a single set of vertical fractures. The fracture density is 0.05, the fracture orientation (normal to fracture symmetry axis orientation) is 0°; The P- and S-wave velocities and density are 4.388 km·s^{-1}, 2.530 km·s^{-1}, 2.800 g·cm^{-3} (Rüger and Tsvankin, 1997); The incident angle ranges from 0° to 50°, and the observed azimuth ranges from 0° to 180°. The normalized AEI calculated using equation (10) is shown in Fig. 1a, the normalized AEI difference is shown in Fig. 1b. We find that the EI variation with azimuth is mainly presented at large incident angles ($\theta>20^{\circ}$). Fig. 1c and d shows $\Delta L_{EI}\Delta L_{EI}{}^{\mathrm{T}}$ and $\Delta L_{EI}{}^{\mathrm{T}}\Delta L_{EI}$ calculated from the normalized AEI difference. We can see that $\Delta L_{EI}\Delta L_{EI}{}^{\mathrm{T}}$ is related to azimuth, both row and column of $\Delta L_{EI}\Delta L_{EI}{}^{\mathrm{T}}$ are functions with a period of π changing with azimuth. Thus, $\Delta L_{EI}\Delta L_{EI}{}^{\mathrm{T}}$ reflects the AVAZ (amplitude variation with angle and azimuth) behavior of the normalized AEI difference. In addition, $\Delta L_{EI}{}^{\mathrm{T}}\Delta L_{EI}$ is related to the incident angle, and reflects the AVA (amplitude variation with angle) behavior of the normalized AEI difference.

The SVD is performed on the normalized AEI difference, and the first three singular values are $d_{11}=1.9316$, $d_{22}=8.5795\times10^{-4}$, and $d_{33}=3.1071\times10^{-15}$, respectively. We find that the first singular value is much larger than the second and third singular values. Due to the rapid reduction of singular values, the first two or three basis functions and singular values are sufficient to accurately recover the normalized AEI difference (Varela, 2009). Fig. 2 shows the first two basis functions obtained from the normalized AEI difference using SVD. We calculate the normalized AEI difference using different basis functions and singular values respectively and obtain the relative error between them and the true value. Fig. 3 shows the relative error between the true value and the normalized AEI difference recovered from different basis functions and singular values. We can see that the relative error between the true value and the normalized AEI difference recovered from the first basis function and singular value is large, while the relative error between the true value and the normalized AEI difference recovered from the first two basis functions and singular values is very small, which indicates that the first two basis functions and

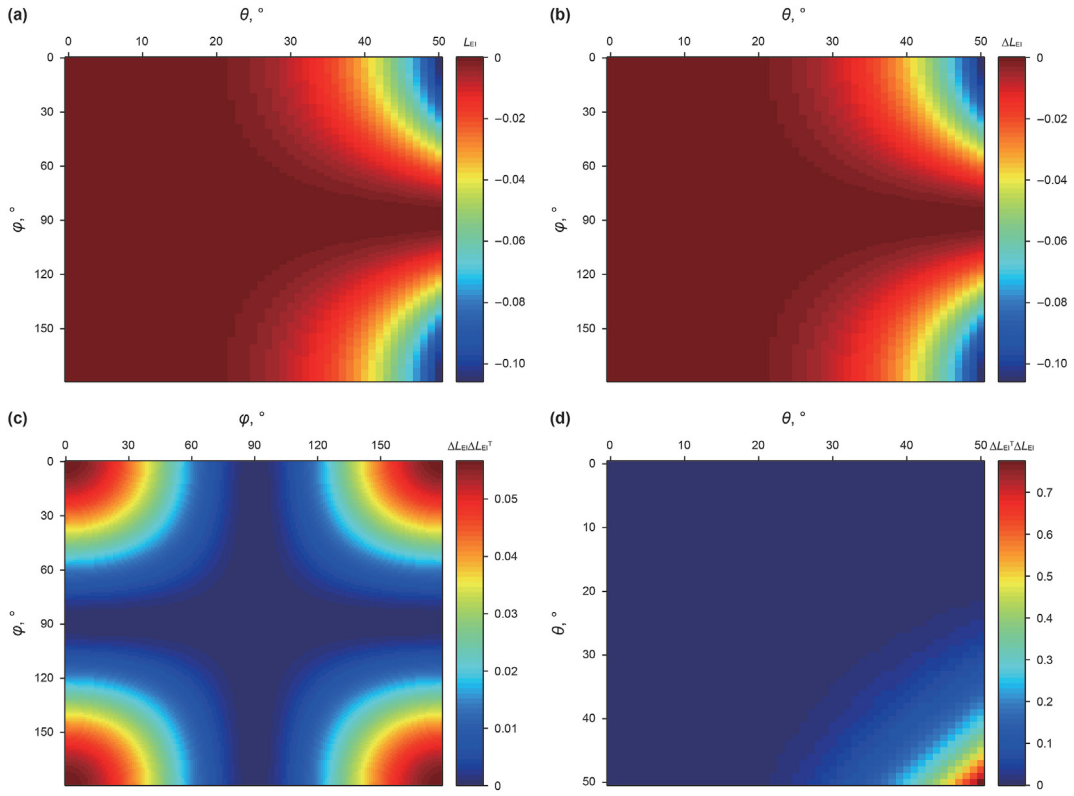

Fig. 1. Synthetic (a) normalized AEI, (b) normalized AEI difference, (c) $\Delta L_{EI}\Delta L_{EI}^{T}$, and (d)$\Delta L_{EI}^{T}\Delta L_{EI}$.

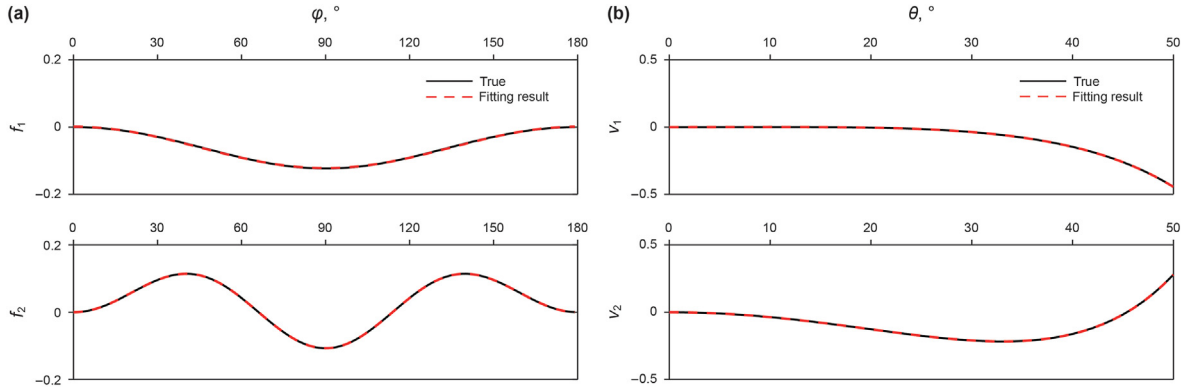

Fig. 2. The first two basis functions obtained from the normalized AEI difference using SVD, where (a) shows basis functions changing with azimuth, and (b) shows basis functions changing with incident angle.

singular values are sufficient to accurately recover the normalized AEI difference. Therefore, equation (13) is simplified to:

$$\Delta L_{EI}(\theta,\varphi) \approx f_1(\varphi)d_{11}(e)v_1(\theta) + f_2(\varphi)d_{22}(e)v_2(\theta) \tag{15}$$

2.3. The relationship between SVD attributes and fracture density and orientation

From Fig. 2a, we find that $f_1(\varphi)$ and $f_2(\varphi)$ are functions with a period of π changing with azimuth, but the trends are different. The peak or trough may directly indicate fracture orientation (0° or 90°). The function that changes periodically with azimuth can be expressed by the Fourier series (Downton et al., 2011) as:

$$f(\varphi) = a_0 + \sum_{n=1}^{\infty}(a_n \cos n\phi + b_n \sin n\phi) \tag{16}$$

where, a_n and b_n represent the nth Fourier coefficients, and fracture symmetry axis azimuth (normal to fracture orientation) can be calculated using

$$\phi_{\text{sym}} = \frac{1}{n}\arctan\left(\frac{b_n}{a_n}\right) \pm 90^{\text{o}} \tag{17}$$

For HTI media with the same symmetry axis, only the $n = 0, 2, 4$ Fourier coefficients are non-zero (Downton and Roure, 2015). Therefore, $f_1(\varphi)$ and $f_2(\varphi)$ can be expressed as:

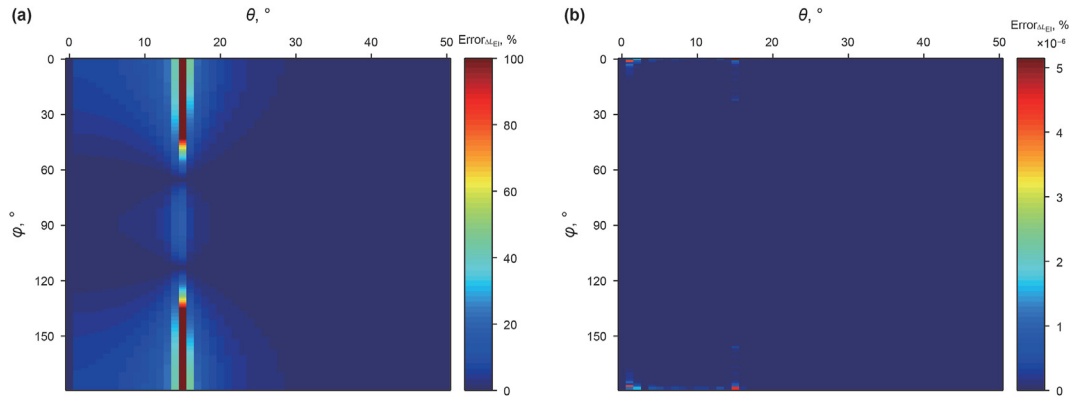

Fig. 3. The relative error between the true value and the normalized AEI difference recovered from different basis functions and singular values, where (a) shows the relative error between the true value and the normalized AEI difference recovered from the first basis functions and singular value, and (b) shows the relative error between the true value and the normalized AEI difference recovered from the first two basis functions and singular values.

$$f_1(\varphi) = a_{f10} + a_{f12}\cos 2\phi + b_{f12}\sin 2\phi + a_{f14}\cos 4\phi + b_{f14}\sin 4\phi \tag{18}$$

$$f_2(\varphi) = a_{f20} + a_{f22}\cos 2\phi + b_{f22}\sin 2\phi + a_{f24}\cos 4\phi + b_{f24}\sin 4\phi \tag{19}$$

From Fig. 2b, we find that $v_1(\theta)$ and $v_2(\theta)$ are functions that vary with incident angle, and reflect the AVA behavior of the normalized AEI difference. Thus, $v_1(\theta)$ and $v_2(\theta)$ can be expressed as:

$$v_1(\theta) = a_{v11}\sin^2\theta + a_{v12}\sin^2\theta\tan^2\theta \tag{20}$$

$$v_2(\theta) = a_{v21}\sin^2\theta + a_{v22}\sin^2\theta\tan^2\theta \tag{21}$$

where, a_{v11}, a_{v12}, a_{v21} and a_{v22} are fitting coefficients.

We use Fourier series to fit $f_1(\varphi)$ and $f_2(\varphi)$, and use basis functions $\sin^2\theta$ and $\sin^2\theta\tan^2\theta$ to fit $v_1(\theta)$ and $v_2(\theta)$, the corresponding results are shown in Fig. 2. We can see that the fitting results (red dashed line) are consistent with the true basis functions (black curve).

Substituting equations (18)–(21) into equation (15) leads to the following expression:

$$\begin{aligned}\Delta L_{EI}(\theta,\varphi) = &\left[\begin{pmatrix} d_{11}a_{f10}a_{v11}+ \\ d_{22}a_{f20}a_{v21}\end{pmatrix} + \begin{pmatrix} d_{11}a_{f12}a_{v11}+ \\ d_{22}a_{f22}a_{v21}\end{pmatrix}\cos 2\phi + \begin{pmatrix} d_{11}b_{f12}a_{v11}+ \\ d_{22}b_{f22}a_{v21}\end{pmatrix}\sin 2\phi\right]\sin^2\theta \\ &+\left[\begin{pmatrix} d_{11}a_{f10}a_{v12}+ \\ d_{22}a_{f20}a_{v22}\end{pmatrix} + \begin{pmatrix} d_{11}a_{f12}a_{v12}+ \\ d_{22}a_{f22}a_{v22}\end{pmatrix}\cos 2\phi + \begin{pmatrix} d_{11}b_{f12}a_{v12}+ \\ d_{22}b_{f22}a_{v22}\end{pmatrix}\sin 2\phi + \begin{pmatrix} d_{11}a_{f14}a_{v12}+ \\ d_{22}a_{f24}a_{v22}\end{pmatrix}\cos 4\phi + \begin{pmatrix} d_{11}b_{f14}a_{v12}+ \\ d_{22}b_{f24}a_{v22}\end{pmatrix}\sin 4\phi\right] \\ &\sin^2\theta\tan^2\theta\end{aligned} \tag{22}$$

Comparing equations (12) and (22) to yield:

$$\begin{aligned} e &= \frac{a_{f12}a_{v11}}{x_1\cos 2\phi_{sym}}d_{11} + \frac{a_{f22}a_{v21}}{x_1\cos 2\phi_{sym}}d_{22} \\ &= \frac{b_{f12}a_{v11}}{x_1\sin 2\phi_{sym}}d_{11} + \frac{b_{f22}a_{v21}}{x_1\sin 2\phi_{sym}}d_{22}\end{aligned} \tag{23}$$

$$\begin{aligned} e &= -\frac{3a_{f12}a_{v12}}{4\cos 2\phi_{sym}}d_{11} - \frac{3a_{f22}a_{v22}}{4\cos 2\phi_{sym}}d_{22} \\ &= -\frac{3b_{f12}a_{v12}}{4\sin 2\phi_{sym}}d_{11} - \frac{3b_{f22}a_{v22}}{4\sin 2\phi_{sym}}d_{22}\end{aligned} \tag{24}$$

$$\begin{aligned} e &= \frac{a_{f14}a_{v12}}{x_2\cos 4\phi_{sym}}d_{11} + \frac{a_{f24}a_{v22}}{x_2\cos 4\phi_{sym}}d_{22} \\ &= \frac{b_{f14}a_{v12}}{x_2\sin 4\phi_{sym}}d_{11} + \frac{b_{f24}a_{v22}}{x_2\sin 4\phi_{sym}}d_{22}\end{aligned} \tag{25}$$

where,

$$x_1 = \frac{4(2g-1)}{3(1-g)} + \frac{16g}{3(3-2g)}$$

$$x_2 = \frac{g(1-2g)}{3(3-2g)(1-g)}$$

Equations (23)–(25) show that fracture density is related to singular values and the fitting coefficients of basis functions. To analyze the relationship between fracture density, singular values, and the fitting coefficients of basis functions, we first combine the elastic parameters of the above single-layer HTI model with a range of fracture densities (increase from 0 to 0.3, in increments of 0.01) to calculate the normalized AEI difference, and then perform SVD on the normalized AEI difference to obtain modeled basis functions and singular values. Fig. 4 shows the basis functions obtained by performing SVD on the synthetic normalized AEI difference in the case of different fracture densities. We can see that all the basis functions do not change with fracture density, which indicates that the fitting coefficients of basis functions are not related to fracture density. Fig. 5 shows singular values obtained by performing SVD on the synthetic normalized AEI difference in the case of different fracture densities. We find that the first and second singular values are linearly related to the fracture density.

Analysis shows that the fitting coefficients of basis functions are not related to fracture density, and singular values are linearly

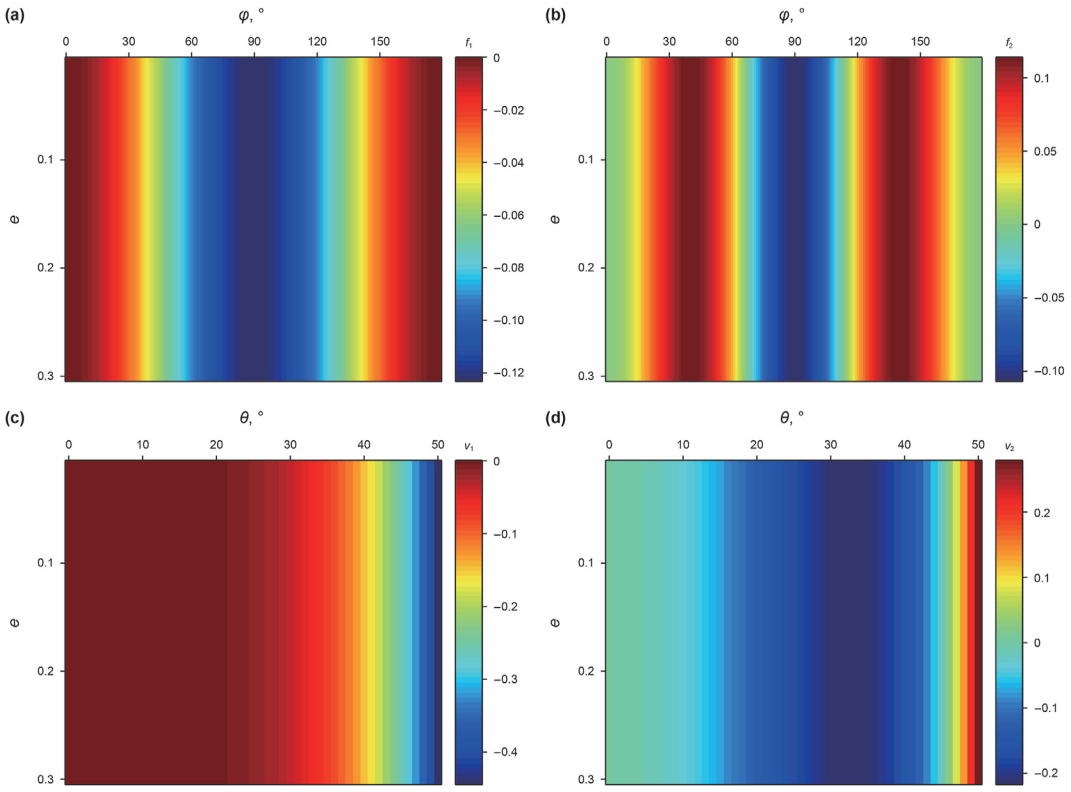

Fig. 4. Basis functions obtained by performing SVD on the synthetic normalized AEI difference in the case of different fracture densities, where (a) shows $f_1(\varphi)$, (b) shows $f_2(\varphi)$, (c) shows $v_1(\theta)$, and (d) shows $v_2(\theta)$.

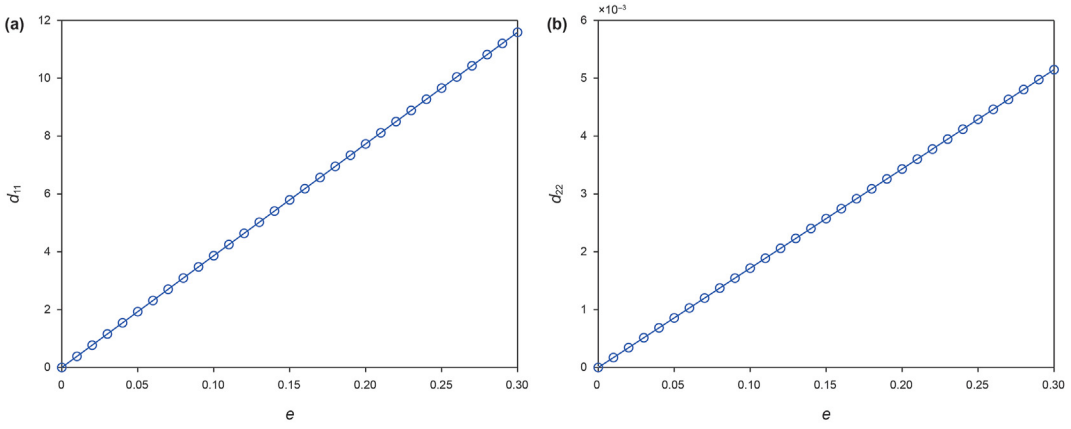

Fig. 5. Singular values obtained by performing SVD on the synthetic normalized AEI difference in the case of different fracture densities, where (a) shows d_{11}, and (b) shows d_{22}.

related to fracture density. Combing equations (23)–(25), we find that there is a relationship between fracture density and singular values as follow

$$e = ad_{11} + bd_{22} \tag{26}$$

Since the first singular value ($d_{11} = 1.9316$) is much larger than the second singular value ($d_{22} = 8.5795 \times 10^{-4}$), the contribution of the second singular value to fracture density is almost negligible, that is, the contribution of singular values to fracture density is mainly from the first singular value. Thus, equation (26) is simplified to

$$e \approx ad_{11} \tag{27}$$

Equation (27) shows that fracture density can be estimated from the modeled relationship between the first singular value and fracture density.

We propose a complete workflow to estimate fracture density and orientation using SVD as follows:

(1) Inversion of AEI. The constrained sparse spike inversion is performed by combining azimuthal angle stacks, azimuthal angle wavelets, and low-frequency models of AEI to obtain the AEI data volume.
(2) Estimation of fracture orientation. We use AEI data volume to calculate the normalized AEI difference, and then perform SVD on the normalized AEI difference to obtain singular

values and basis functions. Furthermore, we perform Fourier series fitting on the first basis function changing with azimuth to estimate the initial fracture orientation. Combing prior fracture orientation information, we obtain the final fracture orientation.

(3) Estimation of fracture density. Combining final fracture orientation and smooth prior ratio g, we calculate the normalized AEI difference using a range of fracture densities and then obtain the relationship between fracture density and the first singular value using SVD. Finally, the estimated first singular value is used to invert fracture density.

3. Examples

3.1. Synthetic examples

We utilize real well logs to generate synthetic data to validate the proposed approach. Fig. 6 shows well logs, including P- and S-wave velocities, density, and fracture density curves. The fracture orientation is assumed to be 0°. Combining well curves and a 30Hz Ricker wavelet, we generate synthetic seismic data based on the convolution model and then add Gaussian noise with an S/N (signal-to-noise) ratio of 2 to synthetic data to simulate observed data. Fig. 7 shows synthetic seismic data with different S/N ratios. Fig. 8 shows the estimated fracture orientation from the first basis function changing with azimuth for different S/N ratios. We observe that the estimated fracture orientations for different S/N ratios are 0°, which are consistent with the true value. Therefore, fracture orientation can be estimated reliably from the first basis function changing with azimuth even when the S/N ratio is 2.

The ratio g needs to be determined before fracture density estimate. To test the influence of the ratio g on the inversion result of fracture density, the true ratio g and the smooth ratio g for 100 times are used to perform fracture density inversion, respectively. Fig. 9 shows the estimated fracture density from the first singular value for synthetic data with different S/N ratios. We observe that both inversion results of fracture density obtained by using the true ratio g (green curve) and the smooth true ratio g (red curve) show good agreement with the true value (black curve) for synthetic data without noise. In the case of S/N ratio being 2, although inversion results of fracture density obtained by using the true ratio g and the smooth true ratio g are slightly different in local areas, both inversion results are consistent with the true value.

In addition, we calculate the correlation coefficient between the true value and inversion result for synthetic data with different S/N ratios, respectively. In the case of synthetic data without noise, the correlation coefficients between the true value and the inversion results obtained from the true ratio g and the smooth ratio g are 0.9714 and 0.9630, respectively. In the case of synthetic data with S/N ratio being 2, the correlation coefficients between the true value and the inversion results obtained from the true ratio g and the smooth ratio g are 0.8574 and 0.8551, respectively; The results show that the correlation coefficient between the true value and the estimated fracture density by the proposed approach is above 0.85 even in the case of S/N ratio being 2. Therefore, fracture density can be reliably estimated from the first singular value provided the smooth prior information of ratio g.

3.2. Field data example

A 3D seismic data set is acquired over the Xinchang gas field in Sichuan Basin. The target is a naturally fractured gas-bearing reservoir in the Xujiahe formation, mainly developed nearly vertical fractures, so reservoirs are equivalent to HTI media. The porosity of the reservoir is generally less than 4%, and the permeability is generally below $0.1 \times 10^{-3}\mu m^2$. Natural fractures

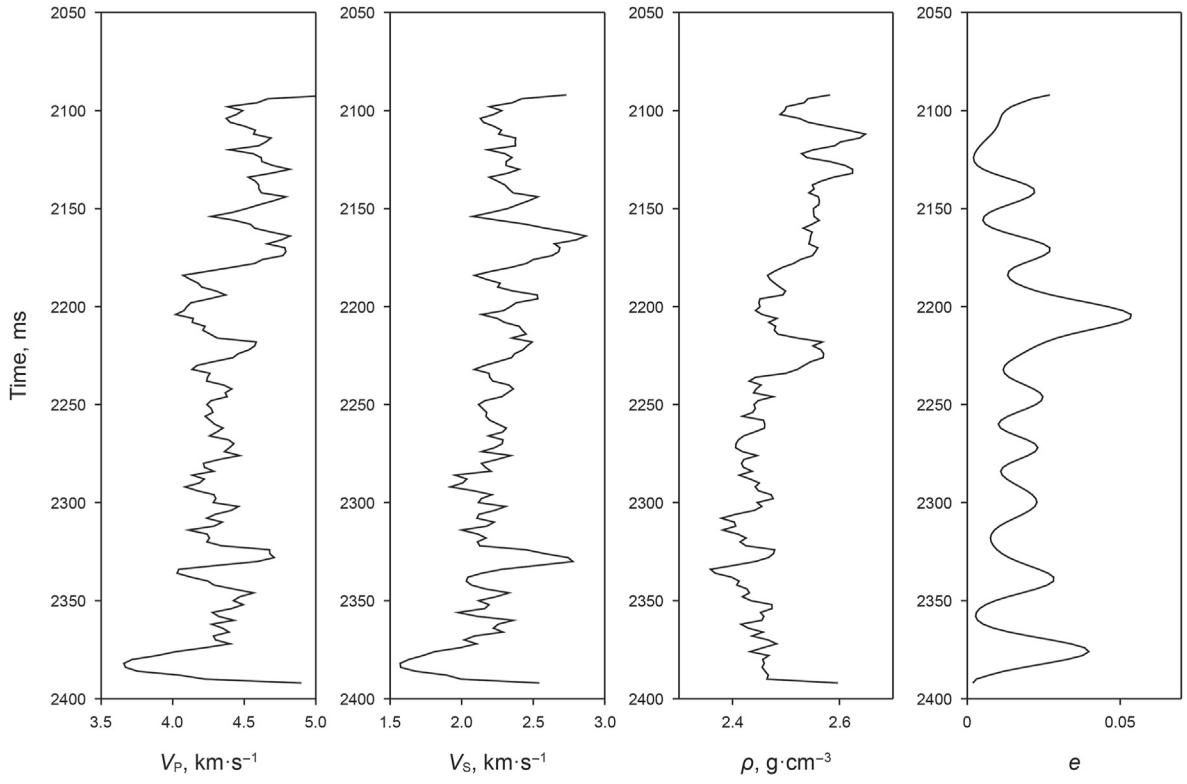

Fig. 6. Well logs.

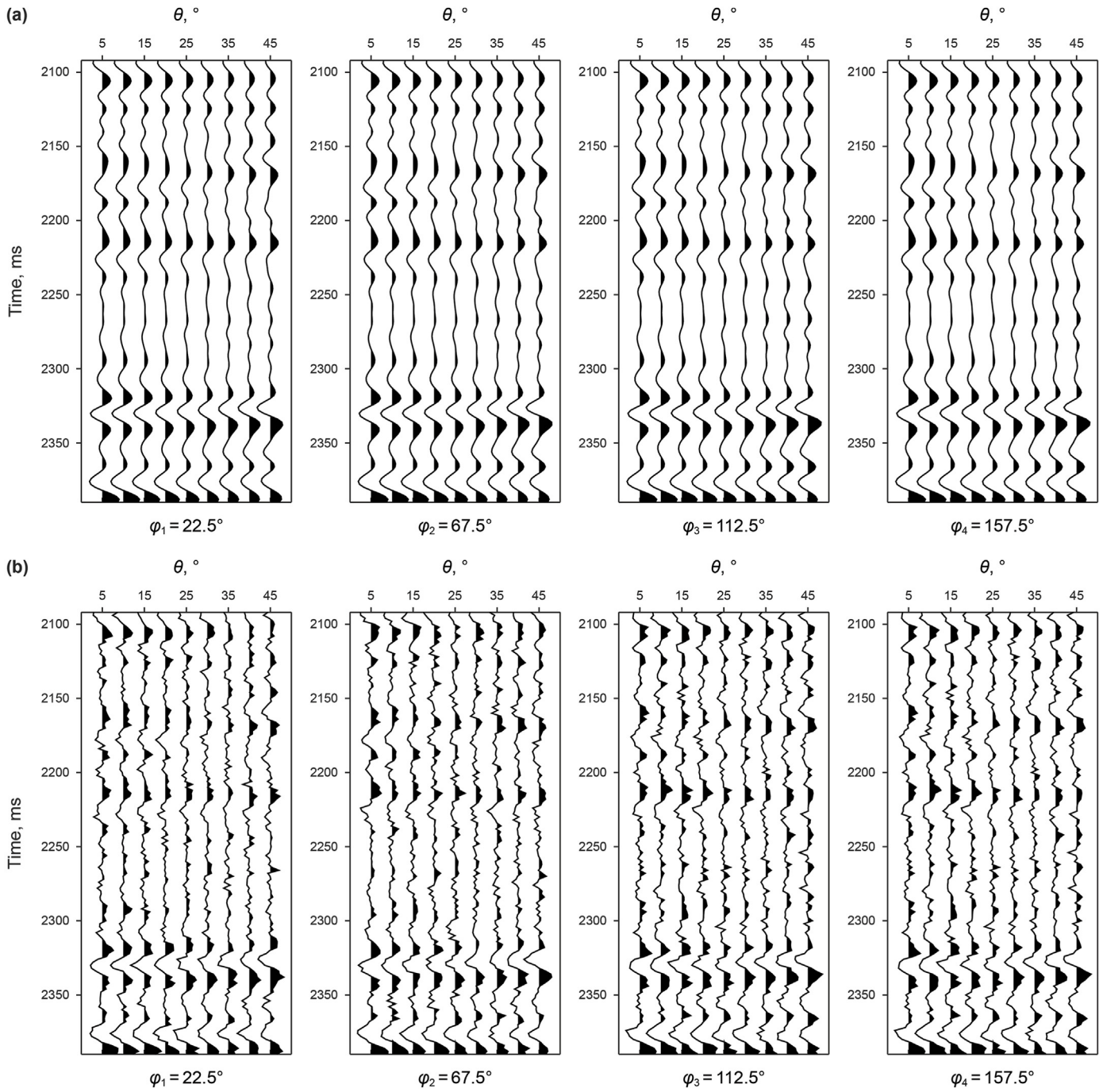

Fig. 7. Synthetic seismic data with different S/N ratios, where (a) shows the case without noise, and (b) shows the case of S/N ratios being 2.

developed in the reservoir contribute little to porosity but have a significant effect on increasing permeability. Relative amplitude-preserved processing is applied to the 3D pre-stack seismic data to preserve the relative azimuthal amplitude variation. Processed data are subdivided into four different source-to-receiver azimuth sectors: 22.5° (0°–45°), 67.5° (45°–90°), 112.5° (90°–135°), and 157.5° (135°–180°). Each azimuth sector is then partially stacked for small incident angle 18° (15°–21°), middle incident angle 22° (19°–25°), and large incident angle 26° (23°–29°).

Fig. 10 shows azimuthal angle stack profiles. We can see that the quality of azimuthal angle stacks at small incident angle is better than that at middle and large incident angles. Fig. 11 shows the inverted AEI profiles obtained by the commercial software Jason. Fig. 12 shows the rose diagram of fracture orientation at the location of well A. We find that the fracture orientation is mainly N60°E. Fig. 13 shows the initially estimated fracture orientation profile. We observe that the initially estimated fracture orientation profile mainly shows N60°E and N150°E, so there is a 90° ambiguity in the initially estimated fracture orientation profile. We use the prior fracture orientation of well A to correct the initially estimated fracture orientation, and obtain the final estimated fracture orientation profile as shown in Fig. 14. We can see that the fracture orientation shown in the final estimated fracture orientation profile is mainly N60°E, and the 90° ambiguity is removed. To verify the

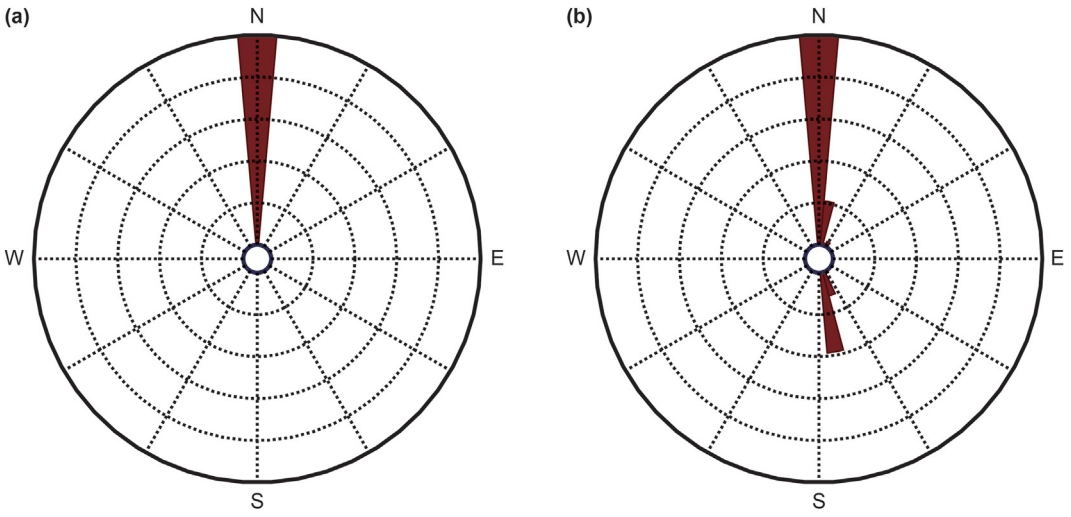

Fig. 8. Estimated fracture orientation from the first basis function changing with azimuth for synthetic data with different S/N ratios, where (a) shows the case without noise, and (b) shows the case of S/N ratio being 2.

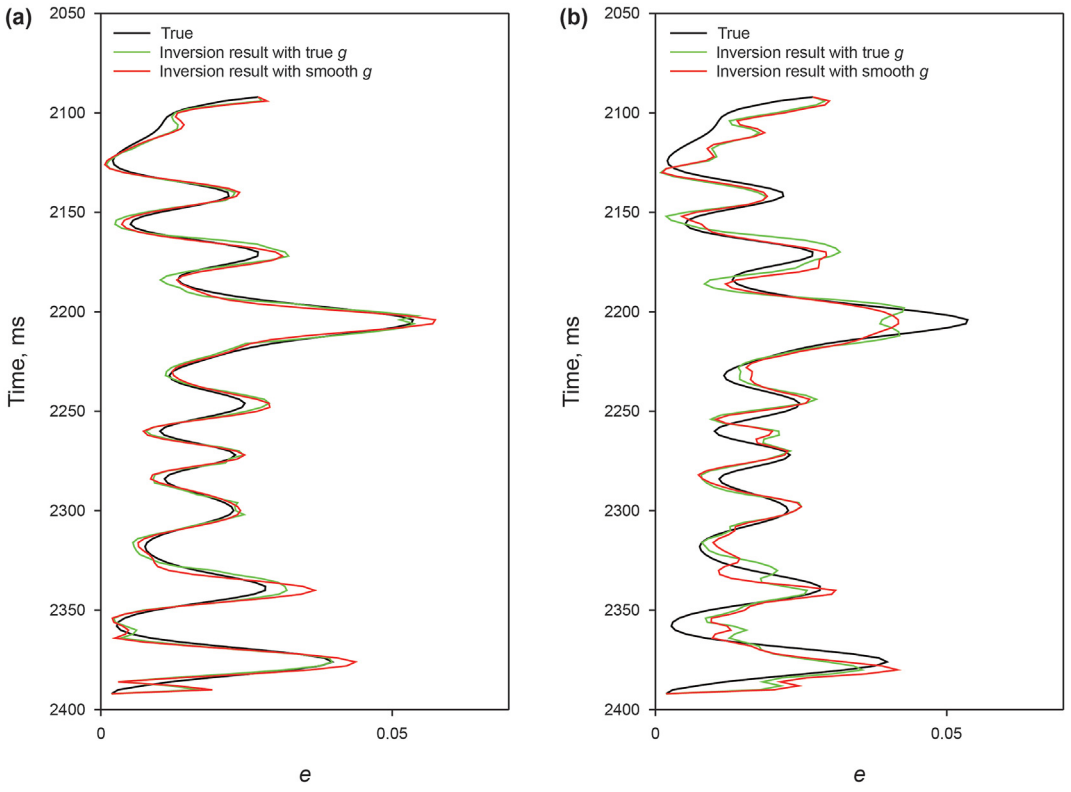

Fig. 9. Estimated fracture density from the first singular value for synthetic data with different S/N ratios, where (a) shows the case without noise, and (b) shows the case of S/N ratio being 2.

reliability of the estimated fracture orientation, the estimated fracture orientation at the location of well A is extracted as shown in Fig. 15. We observe that the estimated fracture orientation at the location of well A is mainly N60°E, which is consistent with image logs at the well (Fig. 12). Fig. 16 shows the estimated fracture density profile. The red ellipse represents fractured gas-bearing reservoirs, and the estimated fracture density shows high-value anomalies, which could reliably indicate fractured gas-bearing reservoirs. Fig. 17 shows the estimated fracture density horizontal slice of HOR in the target zone, the orientations of the black segments represent fracture orientations, which are weighted by fracture density value. Our results indicate that the areas of the highest fracture densities are mainly located in the northwest and north of the study area. Furthermore, we observe that well A is

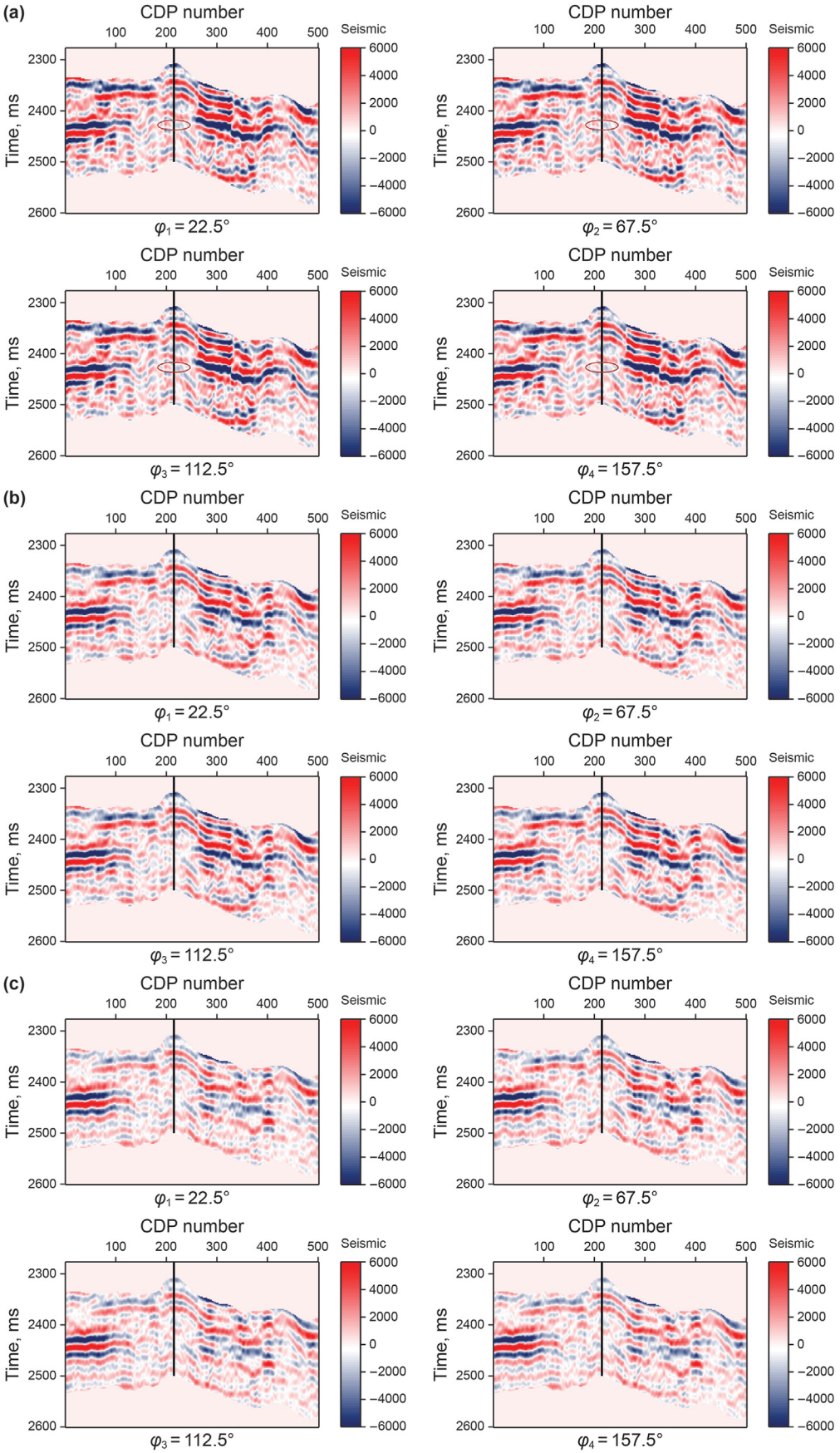

Fig. 10. Azimuthal angle stack profiles, where (a) shows the data at small incident angle 18° (15°–21°), (b) shows the data at middle incident angle 22° (19°–25°), and (c) shows the data at large incident angle 26° (23°–29°). The black curve indicates the location of well A, and the red ellipse indicates the fractured gas-bearing reservoir.

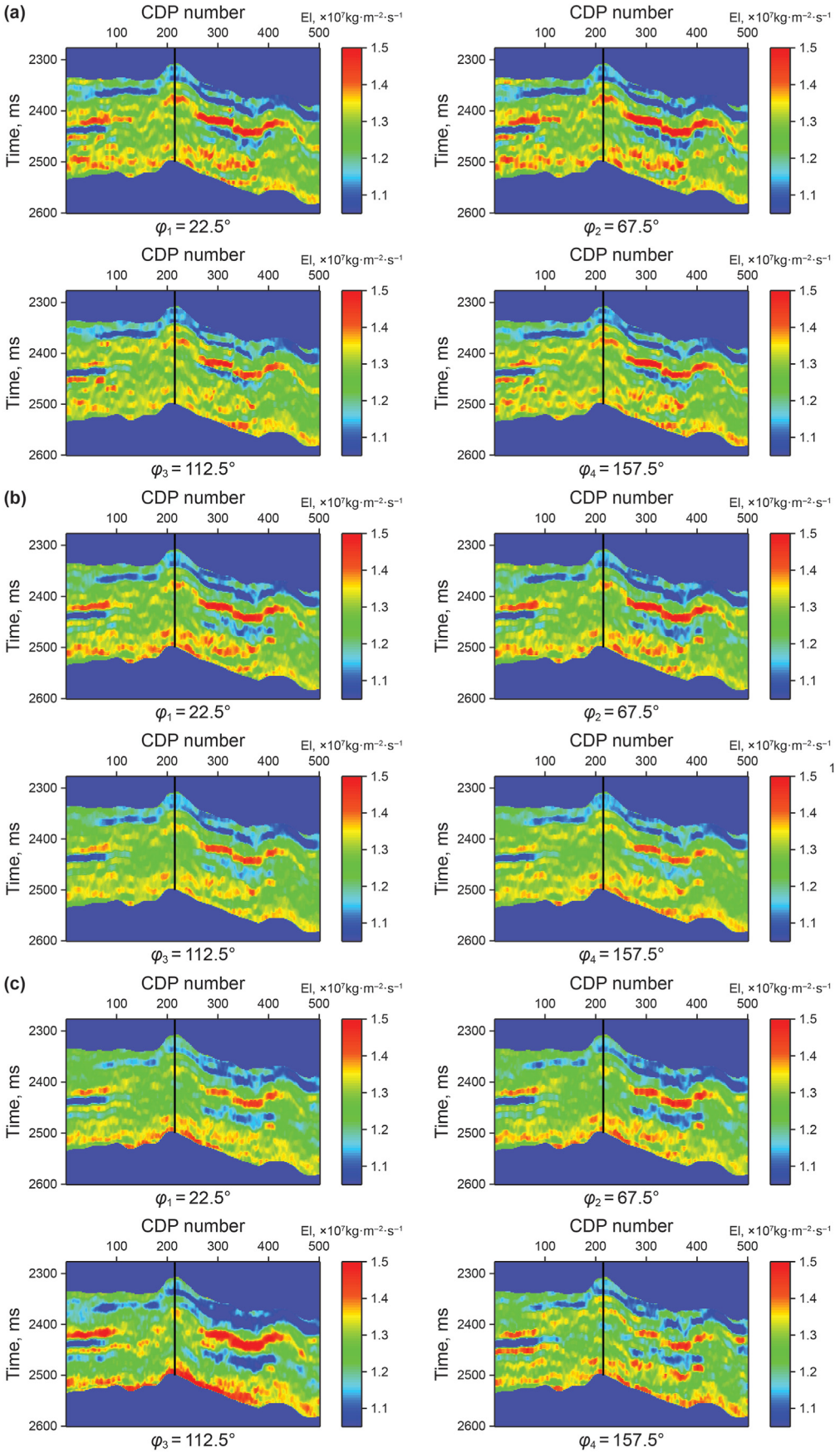

Fig. 11. Inverted AEI profiles, where (a) shows the data at small incident angle 18° (15°–21°), (b) shows the data at middle incident angle 22° (19°–25°), and (c) shows the data at large incident angle 26° (23°–29°).

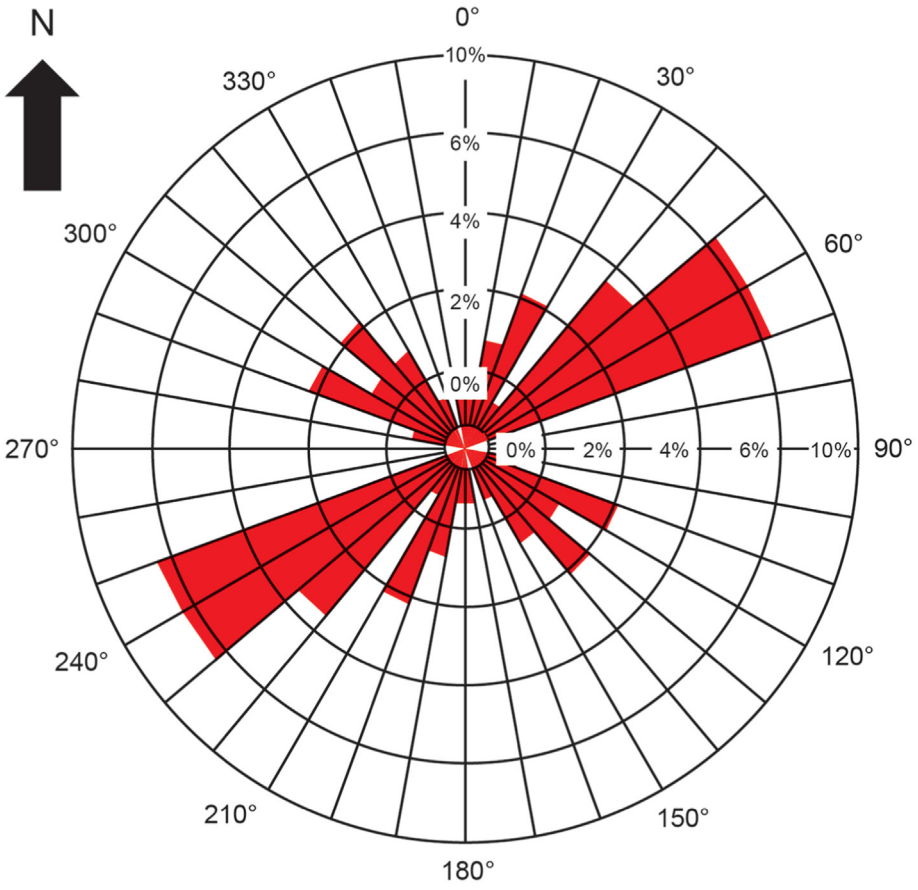

Fig. 12. Rose diagram of fracture orientation at the location of well A.

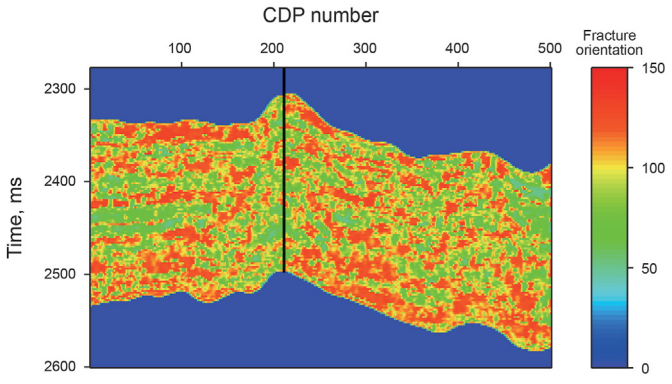

Fig. 13. Initially estimated fracture orientation profile.

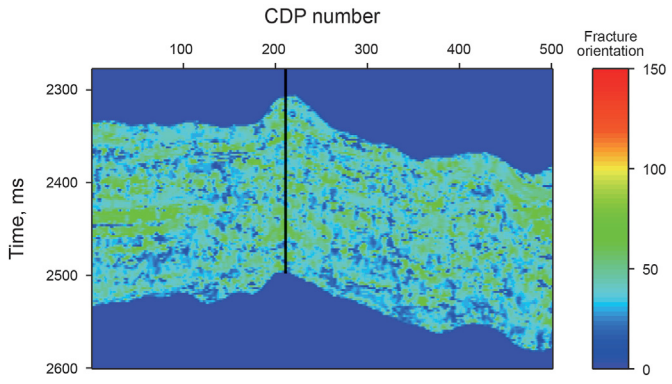

Fig. 14. Final estimated fracture orientation profile.

located in the area with high fracture density, and the estimated fracture orientation nearby well A is mainly N60°E, which is consistent with image log data.

4. Conclusions

Considering HTI media induced by nearly vertical parallel gas-filled fractures, we derive the AEI equation with fracture density and propose a novel approach to estimate fracture density and orientation from the normalized AEI difference using SVD. Analysis shows that the first two basis functions and singular values are sufficient to accurately recover the normalized AEI difference. The basis function changing with azimuth is related to fracture orientation, singular value is linearly related to fracture density; Fracture density is the linearly weighted sum of singular values, and the first singular value contributes the most to fracture density. Synthetic examples demonstrate that fracture orientation can be stably estimated from the first basis function changing with azimuth, fracture density can be reliably estimated from the first singular value provided the smooth prior ratio g, the correlation coefficient between the true value and the estimated fracture density is above 0.85 even in the case of S/N ratio being 2. Field data example shows that the estimated fracture orientation is in agreement with image log data, and the estimated fracture density has good lateral

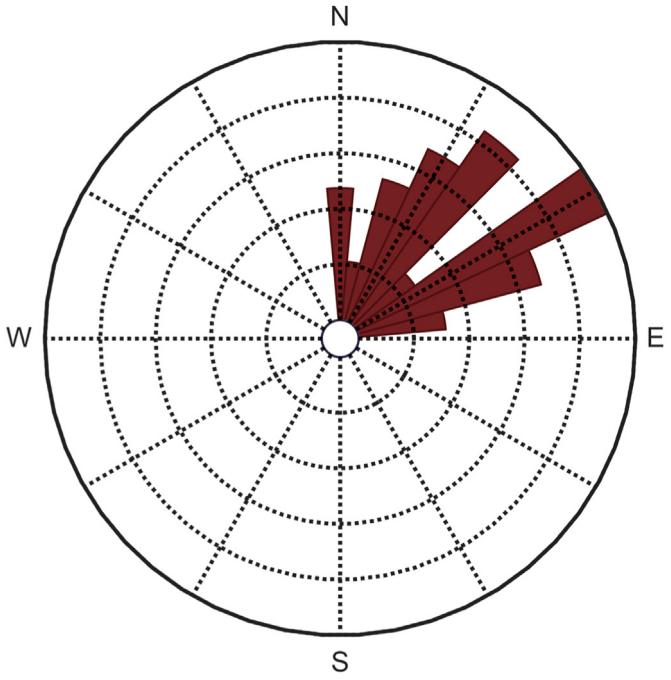

Fig. 15. Estimated fracture orientation at the location of well A.

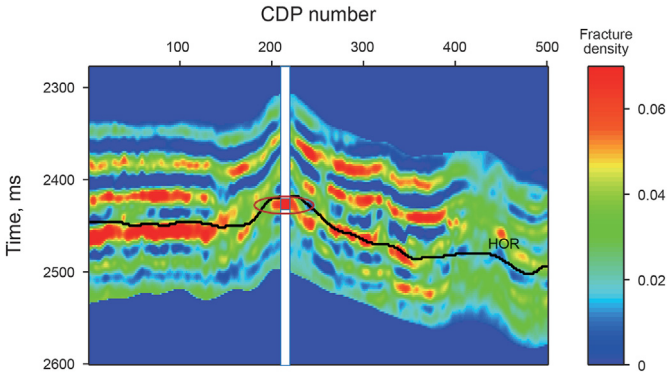

Fig. 16. Estimated fracture density profile. The columnar plotting illustrates the gas-bearing shows.

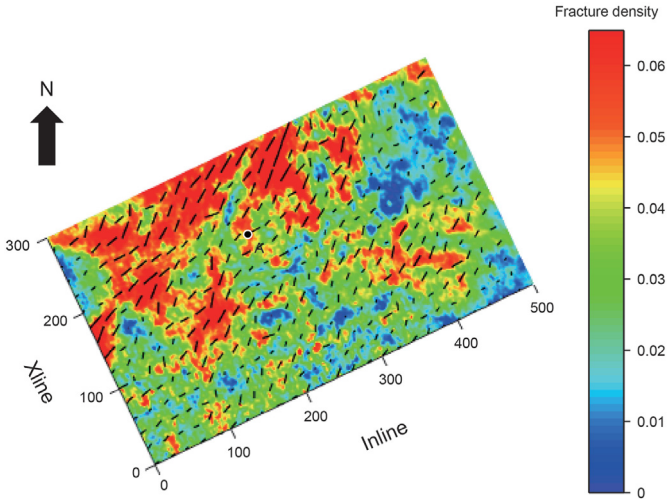

Fig. 17. Estimated fracture density horizontal slice of HOR in the target zone. The orientations of the black segments represent fracture orientations.

continuity and reliably indicates fractured gas-bearing reservoirs, which helps to further identify the lateral distribution of fracture development areas.

Acknowledgements

We would like to express our gratitude for the sponsorship of the National Natural Science Foundation of China (41674130, U19B2008), and the Postgraduate Innovation Project in China University of Petroleum (East China) (YCX2021016) for their funding this research, we gratefully appreciate CGG's university grant program for providing Jason software.

References

Al-Marzoug, A.M., Neves, F.A., Kim, J.J., et al., 2006. P-wave anisotropy from azimuthal AVO and velocity estimates using 3D seismic data from Saudi Arabia. Geophysics 71 (2), E7–E11. https://doi.org/10.1190/1.2187724.

Bakulin, A., Grechka, V., Tsvankin, I., 2000. Estimation of fracture parameters from reflection seismic data—Part I: HTI model due to a single fracture set. Geophysics 65 (6), 1788–1802. https://doi.org/10.1190/1.1444863.

Causse, E., Riede, M., Van Wijngaarden, A., et al., 2007a. Amplitude analysis with an optimal model-based linear AVO approximation: Part I—Theory. Geophysics 72 (3), C59–C69. https://doi.org/10.1190/1.2712176.

Causse, E., Riede, M., Van Wijngaarden, A., et al., 2007b. Amplitude analysis with an optimal model-based linear AVO approximation: Part II—field data example. Geophysics 72 (3), C71–C79. https://doi.org/10.1190/1.2712176.

Chen, H.Z., Yin, X.Y., Gao, J.H., et al., 2015. Seismic inversion for underground fractures detection based on effective anisotropy and fluid substitution. Sci. China Earth Sci. 58 (5), 805–814. https://doi.org/10.1007/s11430-014-5022-1 (in Chinese).

Chen, Z.G., Li, F., Wang, X., et al., 2018. Application of prestack anisotropic intensity attribute in prediction of P Buried hill fractured reservoir in Bongor Basin, Chad. Chin. J. Geophys. 61 (11), 4625–4634. https://doi.org/10.6038/cjg2018L0640 (in Chinese).

Chopra, S., Marfurt, K.J., 2007. Seismic attributes for prospect identification and reservoir characterization. Journal. https://doi.org/10.1190/1.9781560801900.ch18.

Connolly, P., 1999. Elastic impedance. Lead. Edge 18 (4), 438–452. https://doi.org/10.1190/1.1438307.

Downton, J.E., Roure, B., 2015. Interpreting azimuthal Fourier coefficients for anisotropic and fracture parameters. Interpretation 3 (3), ST9–ST27. https://doi.org/10.1190/INT-2014-0235.1.

Downton, J.E., Roure, B., Hunt, L., 2011. Azimuthal fourier coefficients. CSEG Recorder 36 (10), 22–36.

Grechka, V., Tsvankin, I., 1999. 3-D moveout inversion in azimuthally anisotropic media with lateral velocity variation: theory and a case study. Geophysics 64 (4), 1202–1218. https://doi.org/10.1190/1.1444627.

Hudson, J.A., 1981. Wave speeds and attenuation of elastic waves in material containing cracks. Geophys. J. Int. 64 (1), 133–150. https://doi.org/10.1111/j.1365-246X.1981.tb02662.x.

Li, C.P., Yin, X.Y., Liu, Z.G., et al., 2017. An anisotropic gradient inversion for fractured reservoir prediction. Geophys. Prospect. Pet. 56 (6), 835. https://doi.org/10.3969/j.issn.1000-1441.2017.06.009 (in Chinese).

Li, L., Zhang, J.J., Pan, X.P., et al., 2020. Azimuthal elastic impedance-based Fourier coefficient variation with angle inversion for fracture weakness. Petrol. Sci. 17 (1), 86–104. https://doi.org/10.1007/s12182-019-00405-0.

Li, Y.F., Sun, W., Liu, X.W., et al., 2018. Study of the relationship between fractures and highly productive shale gas zones, Longmaxi Formation, Jiaoshiba area in eastern Sichuan. Petrol. Sci. 15 (3), 498–509. https://doi.org/10.1007/s12182-018-0249-7.

Liu, E., Martinez, A., 2013. Seismic Fracture Characterization.

Liu, L.F., Sun, S.Z., Yang, H.J., et al., 2011. Seismic attributes and integrated prediction of fractured and caved carbonate reservoirs in the Tarim Basin, China. Petrol. Sci. 8 (4), 455–461. https://doi.org/10.1007/s12182-011-0163-8.

Liu, Y.W., Liu, X.W., Lu, Y.X., et al., 2018. Fracture prediction approach for oil-bearing reservoirs based on AVAZ attributes in an orthorhombic medium. Petrol. Sci. 15 (3), 510–520. https://doi.org/10.1007/s12182-018-0250-1.

Mallick, S., Craft, K.L., Meister, L.J., et al., 1998. Determination of the principal directions of azimuthal anisotropy from P-wave seismic data. Geophysics 63 (2), 692–706. https://doi.org/10.1190/1.1444369.

Martins, J.L., 2006. Elastic impedance in weakly anisotropic media. Geophysics 71 (3), D73–D83. https://doi.org/10.1190/1.2195448.

Pan, X.P., Zhang, G.Z., 2019. Bayesian seismic inversion for estimating fluid content and fracture parameters in a gas-saturated fractured porous reservoir. Sci. China Earth Sci. 62 (5), 798–811. https://doi.org/10.1007/s11430-018-9284-2.

Pan, X.P., Zhang, G.Z., Chen, H.Z., et al., 2017. McMC-based nonlinear EIVAZ inversion driven by rock physics. J. Geophys. Eng. 14 (2), 368–379. https://doi.org/10.1088/1742-2140/aa5af5.

Pan, X.P., Zhang, G.Z., Yin, X.Y., 2018. Azimuthally pre-stack seismic inversion for

orthorhombic anisotropy driven by rock physics. Sci. China Earth Sci. 61 (4), 425–440. https://doi.org/10.1007/s11430-017-9124-6.
Rüger, A., Tsvankin, I., 1997. Using AVO for fracture detection: analytic basis and practical solutions. Lead. Edge 16 (10), 1429–1434. https://doi.org/10.1190/1.1437466.
Rüger, A., 1998. Variation of P-wave reflectivity with offset and azimuth in anisotropic media. Geophysics 63 (3), 935–947. https://doi.org/10.1190/1.1444405.
Schoenberg, M., 1980. Elastic wave behavior across linear slip interfaces. J. Acoust. Soc. Am. 68 (5), 1516–1521. https://doi.org/10.1121/1.385077.
Schoenberg, M., Sayers, C.M., 1995. Seismic anisotropy of fractured rock. Geophysics 60 (1), 204–211. https://doi.org/10.1190/1.1443748.
Sun, S.Z., Wang, Z.M., Yang, H.J., et al., 2011. P-wave fracture prediction algorithm using pre-stack data with limited azimuth distribution: a case study in the TZ45 area, Tarim Basin, China. Petrol. Sci. 8 (4), 422–432. https://doi.org/10.1007/s12182-011-0160-y.
Varela, I., 2009. Fracture Studies from Amplitude versus Offset and Azimuth and Vertical Seismic Profile Data. Ph.D. Thesis. University of Edinburgh.
Varela, I., Maultzsch, S., Li, X.Y., et al., 2007. Fracture-properties inversion from azimuthal AVO using singular value decomposition. In: 77th SEG Annual Meeting. expanded abstracts, pp. 259–263. https://doi.org/10.1190/1.2792422.
Whitcombe, D.N., 2002. Elastic impedance normalization. Geophysics 67 (1), 60–62. https://doi.org/10.1190/1.1451331.
Yin, X.Y., Zhang, H.X., Zong, Z.Y., 2018. Research status and progress of 5D seismic data interpretation in OVT domain. Geophys. Prospect. Pet. 57 (2), 155–178. https://doi.org/10.3969/j.issn.1000-1441.2018.02.001 (in Chinese).
Yuan, S.Y., Wang, J.H., Liu, T., et al., 2020. 6D phase-difference attributes for wide-azimuth seismic data interpretation. Geophysics 85 (6), IM37–IM49. https://doi.org/10.1190/geo2019-0431.1.
Zhang, G.Z., Chen, H.Z., Yin, X.Y., et al., 2012. Method of fracture elastic parameter inversion based on anisotropic AVO, 871 J. Jilin Univ. (Sci. Ed.) 42 (3), 845–851. https://doi.org/10.3969/j.issn.1671-5888.2012.03.031 (in Chinese).
Zong, Z.Y., Sun, Q.H., Li, C.P., et al., 2018. Young's modulus variation with azimuth for fracture-orientation estimation. Interpretation 6 (4), T809–T818. https://doi.org/10.1190/INT-2017-0101.1.
Zong, Z.Y., Yin, X.Y., Wu, G.C., 2013. Elastic impedance parameterization and inversion with Young's modulus and Poisson's ratio. Geophysics 78 (6), N35–N42. https://doi.org/10.1190/geo2012-0529.1.